Environmental Science and Ecotechnology 20 (2024) 100414

Contents lists available at ScienceDirect

Environmental Science and Ecotechnology

journal homepage: www.journals.elsevier.com/environmental-science-and-ecotechnology/

Original Research

In situ single iron atom doping on Bi_2WO_6 monolayers triggers efficient photo-fenton reaction

Wei Liu [a], Peifang Wang [a], Juan Chen [a], Xin Gao [a], Huinan Che [a], Xiaozhi Su [c], Bin Liu [b], Yanhui Ao [a, *]

[a] *Key Laboratory of Integrated Regulation and Resource Development on Shallow Lakes, Ministry of Education, College of Environment, Hohai University, No.1, Xikang Road, Nanjing, 210098, China*
[b] *School of Chemical and Biomedical Engineering, Nanyang Technological University, Singapore, 637459, Singapore*
[c] *Shanghai Synchrotron Radiation Facility, Shanghai Advanced Research Institute, Chinese Academy of Sciences, Shanghai, 201204, China*

ARTICLE INFO

Article history:
Received 19 October 2023
Received in revised form
8 March 2024
Accepted 8 March 2024

Keywords:
H_2O_2 activation
Water treatment
Bismuth tungstate
Photo-fenton catalysts
Emerging organic pollutants

ABSTRACT

Developing an efficient photocatalytic system for hydrogen peroxide (H_2O_2) activation in Fenton-like processes holds significant promise for advancing water purification technologies. However, challenges such as high carrier recombination rates, limited active sites, and suboptimal H_2O_2 activation efficiency impede optimal performance. Here we show that single-iron-atom dispersed Bi_2WO_6 monolayers (SIAD-BWOM), designed through a facile hydrothermal approach, can offer abundant active sites for H_2O_2 activation. The SIAD-BWOM catalyst demonstrates superior photo-Fenton degradation capabilities, particularly for the persistent pesticide dinotefuran (DNF), showcasing its potential in addressing recalcitrant organic pollutants. We reveal that the incorporation of iron atoms in place of tungsten within the electron-rich $[WO_4]^{2-}$ layers significantly facilitates electron transfer processes and boosts the Fe(II)/Fe(III) cycle efficiency. Complementary experimental investigations and theoretical analyses further elucidate how the atomically dispersed iron induces lattice strain in the Bi_2WO_6 monolayer, thereby modulating the d-band center of iron to improve H_2O_2 adsorption and activation. Our research provides a practical framework for developing advanced photo-Fenton catalysts, which can be used to treat emerging and refractory organic pollutants more effectively.

1. Introduction

The ever-increasing pollution of groundwater or surface water caused by industrialization attracted much attention [1–6]. Particularly, the presence of persistent organic pollutants poses serious risks to aquatic life and public health. In response, there is a pressing need to develop effective catalytic systems capable of degrading these stubborn contaminants, thus contributing to environmental cleanup efforts [7–13]. The photo-Fenton process has been regarded as a green and sustainable catalytic process. It can introduce photogenerated electrons to accelerate the Fe(II)/Fe(III) circulation ($\text{Fe(III)} + e^- \rightarrow \text{Fe(II)}$, $\text{Fe(II)} + H_2O_2 \rightarrow \text{Fe(III)} + \bullet OH$), which effectively promote the rate-limiting step of Fenton reaction [14–17]. Therefore, the key to constructing a high-efficiency photo-Fenton system is developing highly efficient semiconductor materials with abundant active sites and excellent electron transfer ability for H_2O_2 activation [18–22].

Recently, Bi-based two-dimensional (2D) semiconductors have been proposed as ideal candidates for constructing high-efficiency photocatalytic systems thanks to fast charge mobility from bulk to the surface, short electron transmission distance, and excellent support effect [23–26]. As a typical Autryville's phase oxide, monolayer Bi_2WO_6 has been highly sought-after and recognized as a promising visible-light-responsive material. Notably, monolayer Bi_2WO_6 features 2D sandwich-like structured $[BiO]^+$-$[WO_4]^{2-}$-$[BiO]^+$, whereby electrons are forced to the middle $[WO_4]^{2-}$ layer and holes are transferred to the surface $[BiO]^+$ layers [27]. However, the dissociation of sluggish electron-hole pairs and the lack of active sites for the H_2O_2 activation are still key problems that hinder improving photocatalytic efficiency [28–30].

As known, single-atom catalysis featuring abundant exposed surface-active sites, low reaction activation barriers, and maximum

---

* Corresponding author.
E-mail address: andyao@hhu.edu.cn (Y. Ao).

https://doi.org/10.1016/j.ese.2024.100414

atom utilization have been widely investigated in photocatalysis [31–35]. Meanwhile, incorporating isolated transition metals (Fe, Cu, and Co) via heteroatom doping is an effective method for promoting H_2O_2 activation in the Fenton-like reaction process [36–38]. For instance, Su et al. reported that single Fe atoms dispersed on carbon nitride with abundant nitrogen vacancies exhibited high efficiency on H_2O_2 activation under visible light irradiation [39]. Zhan et al. demonstrated that Cu-doped α-Fe_2O_3 can activate H_2O_2 under visible light for organic pollutants degradation, and the introduction of Cu changed the d-band center of Fe to enhance the desorption and activation of H_2O_2 [40]. Designing a high-efficiency photo-Fenton system by introducing the isolated transition metal atom into a monolayer Bi_2WO_6 nanosheet holds significant promise. This approach offers multiple advantages: Firstly, introducing a single atom creates a donor level, improving visible-light absorption and strengthening the transfer of photogenerated electrons for a catalysis reaction. Secondly, the introduced single atoms can serve as active sites for H_2O_2 activation. Lastly, the doped single atoms would optimize the adsorption energy of H_2O_2 and reduce the reaction barriers.

Based on the above discussions, single iron atoms doped Bi_2WO_6 monolayers (SIAD-BWOM-*x*, "*x*" indicates the mol percent of the introduced Fe) were successfully prepared via the bottom-up hydrothermal method (Fig. S1). According to the X-ray absorption fine structure spectroscopy (XAFS), it was discovered that the Fe atoms were atomically dispersed in the SIAD-BWOM-4. It can be seen from the high-resolution transmission electron microscopy (HRTEM) that there are lattice strains in SIAD-BWOM-4 and that they can modulate the d-band center of Fe. In addition, experimental results and density functional theory (DFT) calculation further corroborate that the SIAD-BWOM-4 exhibits good light absorption by ***d-d*** orbit transition and excellent charge transfer ability and

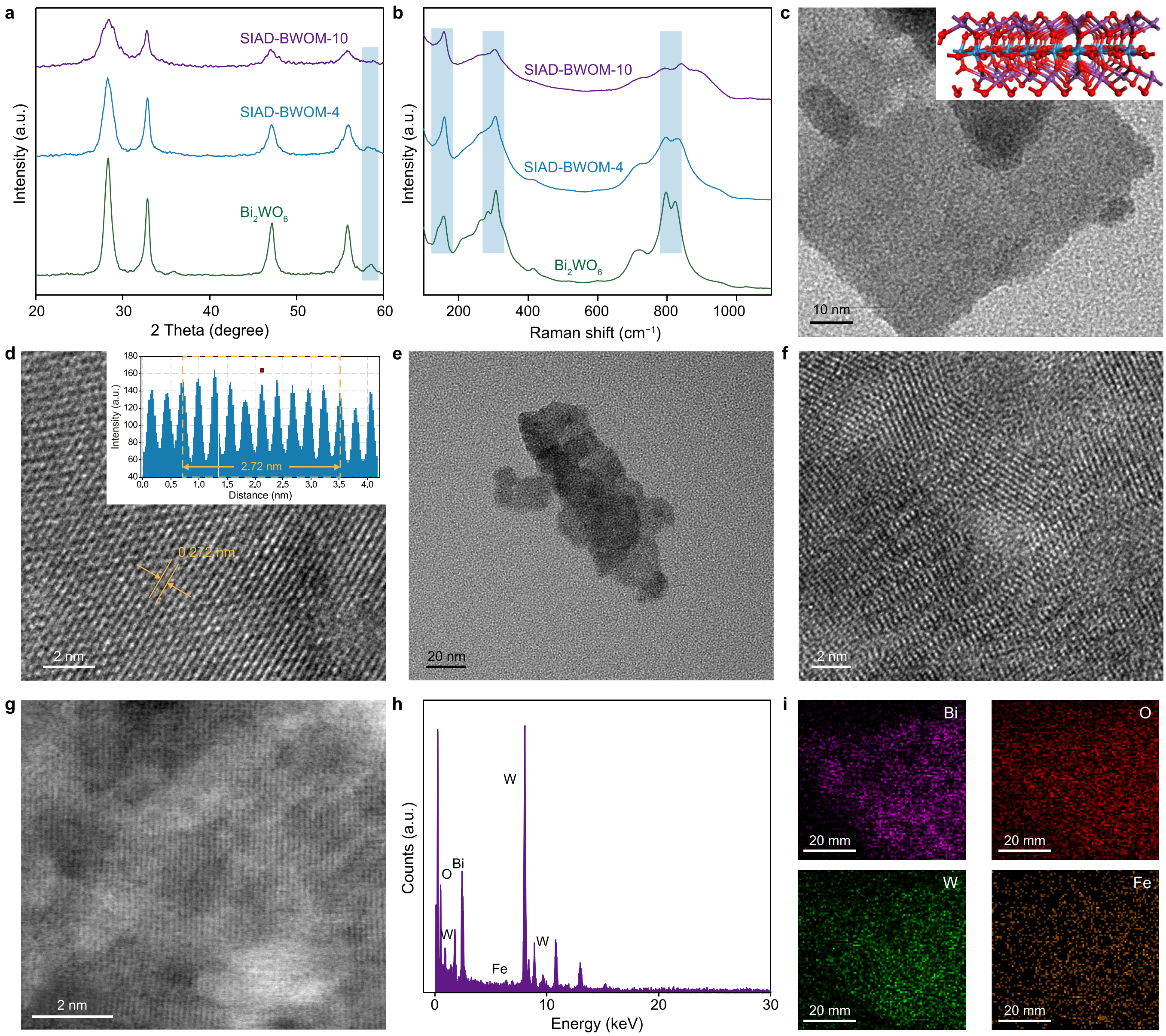

Fig. 1. **a**, XRD pattern of the obtained samples. **b**, Raman spectra of the obtained samples. **c**, TEM image of pure monolayer Bi_2WO_6. **d**, HRTEM image of pure monolayer Bi_2WO_6. **e**, TEM image of SIAD-BWOM-4. **f**, the corresponding HRTEM image of SIAD-BWOM-4. **g**, AC-HAADF-STEM image of ultrathin SIAD-BWOM-4. **h**, EDS of the SIAD-BWOM-4. **i**, EDS mapping images of the SIAD-BWOM-4.

enhances the activation of H_2O_2 by stretching the peroxyl bond. This study can provide a new vision to explore the high-efficiency Photo-Fenton system for contaminant removal.

2. Experiment section

2.1. Materials and reagents

We purchased Bi $(NO_3)_3\cdot5H_2O$, $Na_2WO_4\cdot2H_2O$, Fe $(NO_3)_3\cdot9H_2O$, cetyltrimethylammonium bromide (CTAB), terephthalic acid, ethylene glycol(C_2H_5OH), ammonium oxalate, isopropanol, sodium sulfate (Na_2SO_4), terephthalic acid, 5,5-dimethyl-1-pyrroline N-oxide (DMPO), and hydrogen peroxide solution from Sino Pharm Chemical Reagent Co., Ltd. (China). All chemicals were used without further purification.

2.2. Materials synthesis

In preparing single Fe atom doped Bi_2WO_6 monolayers, 0.05 g CTAB was initially added into 80 mL deionized water, followed by ultrasonic for 30 min. Then, 0.04 mmol Fe $(NO_3)_3\cdot9H_2O$, 2 mmol $Bi(NO_3)_3\cdot5H_2O$, and 1 mmol $Na_2WO_4\cdot2H_2O$ were added into the mixed solution in order. After 1 h stirring, the mixed solution was poured into a 100 mL Teflon-lined autoclave. Then, the autoclave was sealed into a stainless-steel tank and treated at 120 °C for 24 h. Finally, the product was collected and washed several times with deionized water and dried at 60 °C in vacuum. The obtained sample was labeled SIAD-BWOM-4. Subsequently, change the amount of $Fe(NO_3)_3\cdot9H_2O$ to obtain different amounts of Fe-doped Bi_2WO_6 monolayers, labeled as SIAD-BWOM-1, SIAD-BWOM-2, SIAD-BWOM-6, and SIAD-BWOM-10. The pure monolayers Bi_2WO_6 were prepared without Fe $(NO_3)_3\cdot9H_2O$ for comparison. The bulk Bi_2WO_6 and bulk SIAD-BWO-4 were prepared without CTAB assistance.

In addition, detailed characterization techniques, photoelectrochemical measurements, photocatalytic degradation process, and density functional theory are given in the supporting information.

3. Results and discussions

X-ray diffraction (XRD) and Raman spectra were conducted to investigate the structure changes after introducing iron atoms into the Bi_2WO_6 nanosheets. As shown in Fig. 1a and Fig. S2a, all diffraction peaks can be indexed to an orthorhombic Bi_2WO_6 phase (Space group: $Pca2_1$) with lattice parameters of $a = 5.457$ Å, $b = 5.436$ Å, and $c = 16.427$ Å (JCPDS No. 73–2020), while no other phases can be distinguished, demonstrating that there are no extra iron species formed [41]. As shown in Fig. S2b, the (262) peak shows a certain shift in different samples. When the doping amount of iron is low, the (262) peak shifts to a small angle. But when the doping amount of iron is high (such as SIAD-BWOM-10), the dislocation of the internal structure occurs, resulting in the surface relaxation of this peak. In addition, Raman spectra, as a highly sensitive technology for detecting local structure differences, were employed to study the obtained samples. As observed in Fig. S2c, the peaks observed at 157 and 305 cm^{-1} were attributed to the stretching or bending modes of BiO polyhedron and Bi—O bonds, respectively. It is obvious that the Fe doping doesn't change the surface $[BiO]^+$ layers. Therefore, the iron atoms are not doped in $[BiO]^+$ layers. Afterward, as shown in Fig. 1b and Fig. S2d, the peaks near 793 and 822 cm^{-1} correspond to the asymmetric and symmetric stretching vibration of O—W—O, respectively. The other high-energy Raman peak at 720 cm^{-1} is also W-related, originating from an antisymmetric bridging mode associated with the tungstate chain [42]. Interestingly, the stretching vibration of O—W—O and the peak about the tungstate chain have significantly weakened, resulting from substituting the tungsten with iron single atoms.

Transmission electron microscopy (TEM) was utilized to observe the morphology of the obtained samples. As shown in Fig. 1c and d, the pristine monolayer Bi_2WO_6 possesses a sheet-shaped structure with a size of about 50 nm and a thickness of about 1 nm (Fig. S3), which confirms monolayer Bi_2WO_6 nanosheets grow along [001] direction. Fig. 1d gives the corresponding high-resolution transmission electron microscopy (HR-TEM) images, and the lattice spacing of 0.272 nm is consistent with the (020) crystal plane of Bi_2WO_6. The introduction of Fe does not change the morphology of monolayer Bi_2WO_6 (Fig. 1e and f; Fig. S4). Meanwhile, clear lattice strain can be observed in the ultrathin SIAD-BWOM-4 nanosheets. The AC-HAADF-STEM image shows the structure at atomic scale for ultrathin SIAD-BWOM-4 nanosheet (Fig. 1g). According to the EDS (Fig. 1h) and EDS mapping (Fig. 1i), the Bi, W, O, and Fe are uniformly distributed in ultrathin SIAD-BWOM-4, which manifests the presence of Fe element in monolayer Bi_2WO_6 nanosheets.

As shown in Fig. 2a, the absorption edge of SIAD-BWOM-4 was located between those of Fe_2O_3 and FeO in the Fe K-edge X-ray absorption near-edge structure (XANES) spectra, indicating the oxidation state of the Fe in SIAD-BWOM-4 ($Fe^{\delta+}$, $2 < \delta < 3$). The Fourier-transform extended X-ray absorption fine structure (FT-EXAFS) spectrum (Fig. 2b; Fig. S7) of SIAD-BWOM-4 exhibits a solitary peak at approximately 1.49 Å, which is attributed to the Fe—O bond, and no other peaks can be detected. The Fe foil shows the main peak at approximately 2.13 Å, which is attributable to the Fe—Fe interaction peak. In comparison to Fe foil, FeO, and Fe_2O_3, no Fe—Fe peaks were observed, excluding the possibility of any Fe nanoparticles or clusters in SIAD-BWOM-4. Notably, the SIAD-BWOM-10 also has a peak at 2.13 Å, suggesting that there is an iron cluster. In the wavelet transform (WT) contour plots (Fig. 2c), the intensity maxima of Fe foil at 7.41 $Å^{-1}$ is attributed to the Fe—Fe interaction. In addition, a solitary intensity maximum of SIAD-BWOM-4 at 4.17 $Å^{-1}$ can be ascribed to the Fe—O bond. The above results indicated that the Fe atom in SIAD-BWOM-4 was

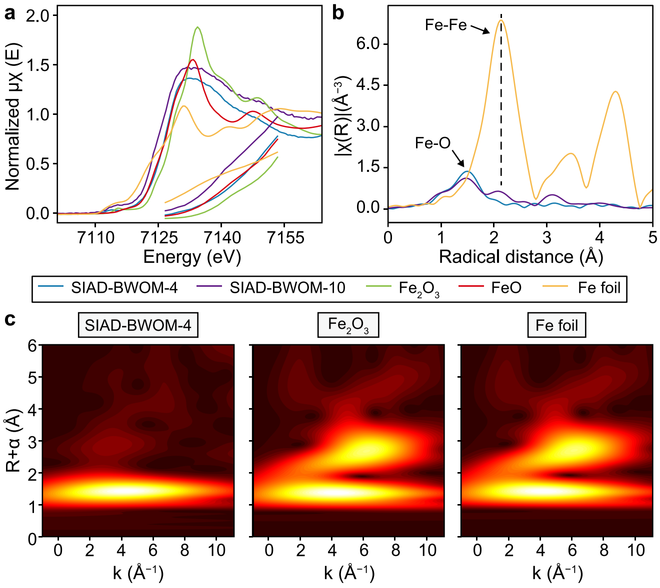

Fig. 2. **a**, Normalized Fe K-edge XANES spectra of different samples. **b**, k^3-weighted Fourier transform spectra of different samples. **c**, WT-EXAFS of Fe K-edge for SIAD-BWOM-4, Fe_2O_3, and Fe foil.

atomically dispersed.

To investigate the change of electron structure along with the introduction of iron single atoms, we conducted X-ray photoelectron spectroscopy (XPS) [43,44]. As shown in Fig. 3a, two characteristic peaks of pure Bi_2WO_6 are located at 37.45 and 35.33 eV, assigned to W $4f_{5/2}$ and W $4f_{7/2}$, respectively. Conspicuously, the W 4f peaks of SIAD-BWOM-4 and SIAD-BWOM-10 shift to low binding energy relative to pure Bi_2WO_6, resulting from the higher electron density after introducing the iron atom. The O 1s spectra of SIAD-BWOM-4 were located at 530.03 and 531.20 eV, ascribing to lattice oxygen and physiosorbed water or surface hydroxyl (Fig. 3b). For Bi 4f XPS spectra (Fig. 3c), two characteristic peaks of original Bi_2WO_6 located at 159.01 and 164.35 eV were assigned to Bi $4f_{7/2}$ and Bi $4f_{5/2}$ of Bi^{3+} ions, respectively. As presented in Fig. 3d, the weak signals (710.67 eV) can be observed in SIAD-BWOM-4, indicating the successful introduction of iron atoms in SIAD-BWOM-4 [45,46]. In addition, the *in situ* irradiated XPS spectra exhibit the binding energy of W 4f, O 1s, and Bi 4f for the SIAD-BWOM-4 sample shift to high energies under light irradiation vs. in the dark, suggesting that the SIAD-BWOM-4 can be excited easily to produce photogenerated electrons under light. As a result, the atomically dispersed iron can capture the photogenerated electron to speed up the Fe(II)/Fe(III) circulation.

As shown in Figs. S8 and S9, and Table S1, the DFT calculation, based on the Fukui index, was employed to unravel the reaction site on DNF. This analysis revealed that DNF, a type of persistent pesticide, was found to have reaction sites readily susceptible to attack by •OH [47]. Subsequently, the photo-Fenton performance of as-obtained material was evaluated via the removal of DNF. As shown in Fig. 4a and Fig. S10, with the addition of H_2O_2, the pure Bi_2WO_6 presents only 18% degradation efficiency, and the bulk SIAD-BWO-4 has almost no degradation efficiency. Interestingly, SIAD-BWOM-4 exhibits remarkable photo-Fenton degradation performance with 60% degradation efficiency. In addition, the low content of iron-doped Bi_2WO_6 nanosheets can also present certain photo-Fenton degradation activity (Fig. S11). This result corroborates the incorporation of the iron atom in monolayer Bi_2WO_6 to capture photogenerated electrons, thus activating H_2O_2 to trigger an efficient photo-Fenton reaction. Unfortunately, as the doping amount of iron increases, the SIAD-BWOM-10 exhibited a sharp decrease in photocatalytic performance since the formation of extra products (such as iron cluster) on the Bi_2WO_6 was not conducive to the activation of H_2O_2, consistent with the XAFS analysis and TEM result. Furthermore, free radical trapping experiments were performed to ascertain the dominant reactive species in such a photo-Fenton system by employing isopropanol (IPA), ammonium oxalate, and Ar. As presented in Fig. 4b, the degradation efficiency of DNF presented a sharp decrease from 60% to 19% with the addition of IPA, and the relative contribution of •OH to the overall DNF degradation was estimated to be 77%. This result indicated that the hydroxyl radicals play a major role in DNF degradation. Eventually, the effect of H_2O_2 concentration on catalyst activity and the possible degradation pathway of DNF were shown in Figs. S12 and S13, respectively.

The ESR measurements using 5,5-dimethyl-1-pyrroline N-oxide (DMPO) as radical trapping agents were employed to research the production of •OH with as-prepared photocatalysts in the photo-Fenton system. Fig. S14 presented the intensity change of the DMPO signal in four systems (SIAD-BWOM-4+H_2O_2, Bi_2WO_6+H_2O_2, SIAD-BWOM-4, and Bi_2WO_6) under different illumination of time and the DMPO-•OH adduct signal with 1:2:2:1 quartet characteristic. This result indicates that Bi_2WO_6 and SIAD-BWOM-4 have a very weak ability to produce •OH. Subsequently, with the addition of H_2O_2, the DMPO-•OH adduct signal is enhanced obviously. Fig. 4c shows the changes in hydroxyl radicals produced in four systems after 8 min of illumination. The signals for the SIAD-BWOM-4 + H_2O_2 system presented remarkably enhanced results in comparison with Bi_2WO_6 + H_2O_2 and SIAD-BWOM-4.

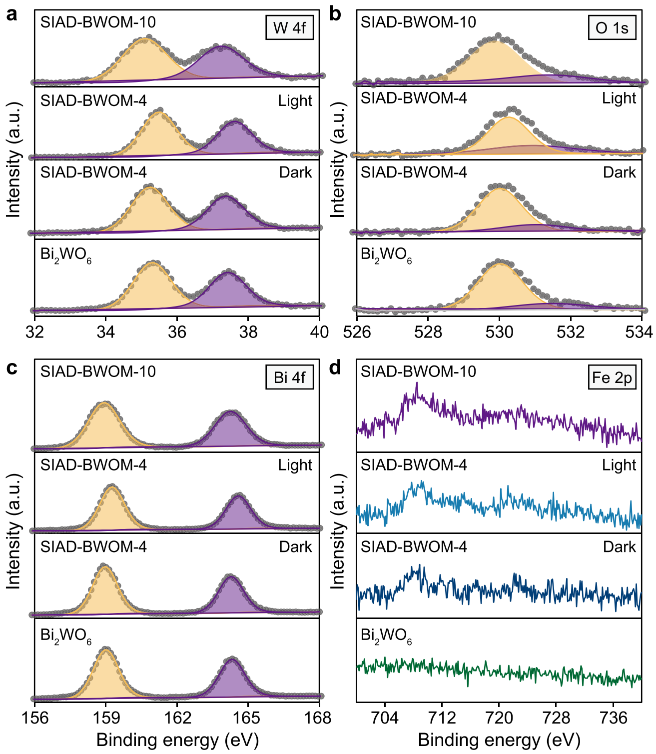

Fig. 3. High-resolution XPS spectra of W 4f (**a**), O 1s (**b**), Bi 4f (**c**), and deconvoluted Fe 2p (**d**).

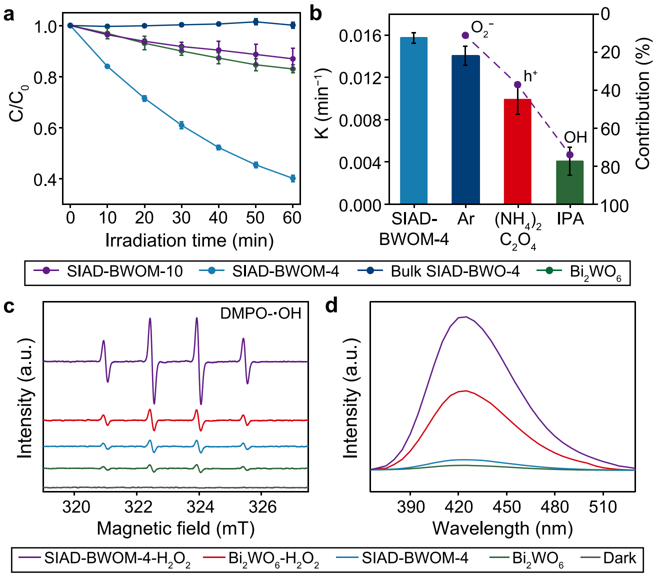

Fig. 4. a, The photo-Fenton activity of as-obtained samples with addition of H_2O_2. **b**, The influence of radical scavenger to DNF photo-Fenton degradation over SIAD-BWOM-4. **c**, DMSO spin-trapping ESR spectra of four different systems: Bi_2WO_6, SIAD-BWOM-4, Bi_2WO_6 + H_2O_2, and SIAD-BWOM-4 + H_2O_2. **d**, Photoluminescence spectra of terephthalic acid mixed with different systems under visible light irradiation. Experiment condition: [catalyst] = 0.5 g L^{-1}, [DNF] = 2 mg L^{-1}, [Degradation volume] = 50 mL, [H_2O_2] = 3.9 mM, [the volume of reactor] = 100 mL, [the intensity of light] = 21.7 mW cm^{-2}, $\lambda \geq 420$ nm, [$(NH_4)_2C_2O_4$] = 1 mM, [IPA] = 1 mM.

Furthermore, we performed a detection assay of •OH in the photo-Fenton system by Photoluminescence (PL) spectra of terephthalic acid [48]. The terephthalic acid could react with •OH to form the hydroxy terephthalic acid with strong PL signals at ~426 nm, as shown in Fig. 4d. The neglectable generation of •OH was found in the only presence of Bi_2WO_6 and SIAD-BWOM-4. However, with the addition of H_2O_2, both Bi_2WO_6 and SIAD-BWOM-4 exhibited enhanced PL signals. And the signal intensity of hydroxy terephthalic acid following the order SIAD-BWOM-4+H_2O_2 > Bi_2WO_6+H_2O_2 > SIAD-BWOM-4 > Bi_2WO_6. This ESR and PL result is consistent with the degradation results and confirms that SIAD-BWOM-4 can quickly activate H_2O_2 to produce •OH.

As known, the light absorption of material is a key factor affecting photocatalytic performance [49]. As shown in Fig. 5a,

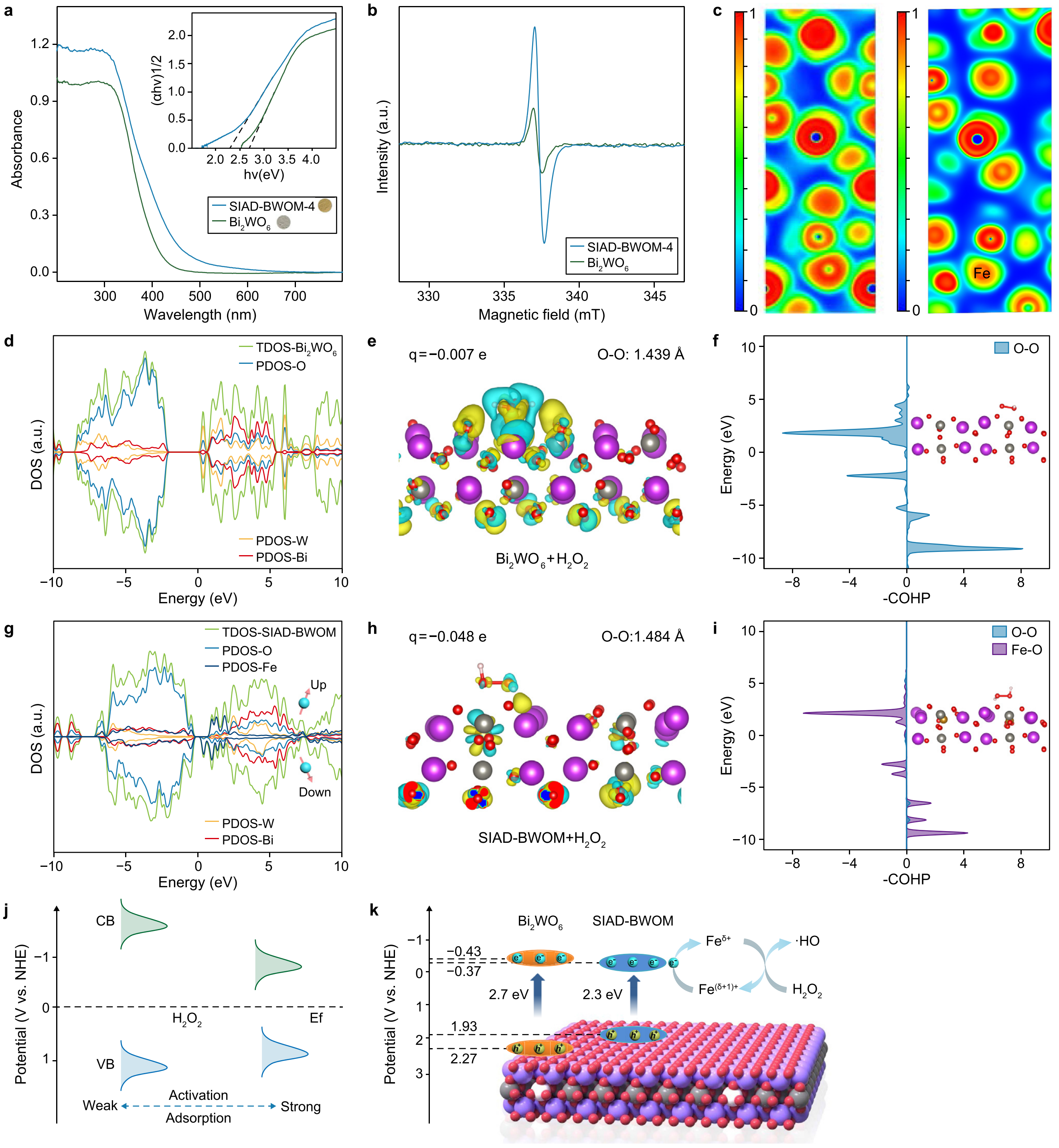

Fig. 5. **a**, UV−vis absorption spectrum. The colors of the as-obtained materials are included next to the caption. The inserted figure is the Tauc plot. **b**, EPR spectra of Bi_2WO_6 and SIAD-BWOM-4. **c**, Electronic localization function (left: Bi_2WO_6; right: SIAD-BWOM-4). **d**,**g**, Calculated DOS of Bi_2WO_6 (**d**) and ultrathin SIAD-BWOM-4 (**g**). **e**,**h**, The different charge densities of H_2O_2 adsorbed on Bi_2WO_6 (**e**) and SIAD-BWOM (**h**). **f**, **i**, COHP of Bi_2WO_6 + H_2O_2 (**f**) and SIAD-BWOM-4+H_2O_2 (**i**). **j**, Schematic diagram of energy level structure. **k**, The photo-Fenton mechanism diagram for SIAD-BWOM-4.

SIAD-BWOM-4 shows enhanced visible-light absorption, as evidenced by its yellow color, in contrast to the white color of pure Bi_2WO_6 (inserted in Fig. 5a). This color change is attributed to ***d-d*** transitions of the dopant iron single atom. Meanwhile, pure Bi_2WO_6 and SIAD-BWOM-4 calculated bandgap values of 2.7 and 2.3 eV, respectively. In addition, the Mott-Schottky, VB-XPS curves, and band position are shown in Fig. S15, echoing the above analysis well. Combined with the EPR spectra (Fig. 5b), it is reasonable to conclude that the isolated iron atom can accumulate more unpaired electrons. Additionally, SIAD-BWOM-4 had a shorter average decay lifetime (1.6 ns, Fig. S16 and Table S2) compared with monolayer Bi_2WO_6 (1.63 ns), demonstrating that the photogenerated electrons should be quickly trapped to activate H_2O_2 molecule thereby decreasing the lifetime of electrons [50,51]. Meanwhile, the photocurrent and electrochemical impedance spectra (EIS) measurements were conducted to investigate the transfer efficiency of the photogenerated electron. As shown in Fig. S17, the high photocurrent response and small EIS arc of SIAD-BWOM-4 suggest that the electron migration speed of SIAD-BWOM-4 is faster, mainly resulting from introducing a Fe single atom [52,53].

To further unveil the fundamental origins of the high photo-Fenton degradation performance of SIAD-BWOM-4 catalyst, DFT calculations were subsequently performed [54]. Firstly, electronic localization function (ELF) and charge density exhibit the charge distribution difference after introducing a single iron atom (Fig. 5c; Fig. S18). The corresponding densities of states (DOS) are shown in Fig. 5d and g. For the pure monolayer Bi_2WO_6, the top of the valence band and the bottom of the conduction band mainly originated from hybrid Bi 6***s***-O 2***p*** orbital and W 5***d***-O 2***p*** orbital, respectively. Compared with the pure Bi_2WO_6, a decreased total density of states is observed at the conduction band minimum after iron atom doping, leading to an easier transfer of photogenerated electrons from Bi_2WO_6 to Fe centers. These occupied states of Fe largely turn into “electron traps” for Bi_2WO_6. As shown from the calculated projected density of states (PDOS) of Fe atoms, introducing Fe can lead to the mismatch between spin up and spin down, thus conducting electron transfer. These results demonstrate the strong electronic coupling between the isolated Fe atoms and the support and verify that the Fe decoration can accelerate the electron transfer with a narrower bandgap [55]. The differential electron density clearly illustrates that the electrons are expected to be transferred into the orbitals of H_2O_2 molecules for H_2O_2 activation. The SIAD-BWOM-4+H_2O_2 system has more electrons ($q = -0.048e$) than Bi_2WO_6+H_2O_2 (Fig. 5e–h). In addition, due to the existence of lattice strain, the d-band center of transition metal Fe can be modulated. As a result, the H_2O_2 molecule was easily adsorbed and activated by the SIAD-BWOM-4, and the peroxide bond (1.484 Å) will be elongated and more easily broken to form •OH. Furthermore, the crystal orbital Hamilton populations (COHP) of H_2O_2 adsorbed on Bi_2WO_6 and SIAD-BWOM were calculated (Fig. 5f–i). The ICOHP showed that the intensity of the Fe–O bond from H_2O_2 adsorbed on SIAD-BWOM (-ICOHP = 0.12), indicating the lattice strain can adsorb and effectively activate the H_2O_2 molecule.

The above results and analysis proposed a more plausible mechanism for the enhanced photo-Fenton performance of the SIAD-BWOM-4 catalyst. Possible band change and reaction process are schematically exhibited in Fig. 5j and k. Introducing isolated Fe atoms can decrease the band gap and enhance visible-light absorption via ***d-d*** transition compared with pure monolayer Bi_2WO_6. Additionally, surface lattice strain may adjust the d-band center of Fe, enhancing the adsorption and activation of the H_2O_2 molecule. Consequently, these modifications significantly boost the photo-Fenton reaction's ability to refractory dinotefuran degradation.

4. Conclusions

In conclusion, the SIAD-BWOM-4 catalyst, synthesized via the bottom-up hydrothermal method, exhibits excellent photo-Fenton degradation performance for DNF. Raman and XAFS analyses revealed that single iron atoms were doped in the subsurface layer $[WO_4]^{2-}$ of Bi_2WO_6, forming the lattice strain. Experimental findings and DFT analysis indicated that isolated Fe sites could optimize visible-light absorption by ***d-d*** transition and serve as an “electron trap” to speed up the photogenerated carrier transfer. Meanwhile, the lattice strain on its surface can modulate the d-band center of Fe, enhancing the adsorption and activation of H_2O_2. The photogenerated electron can be quickly captured to activate the H_2O_2 molecule to improve reaction dynamics. This study provides new horizons for effectively treating pesticides by building the interaction relationship between catalysis system design, free radical generation, and pollutant molecules.

CRediT authorship contribution statement

Wei Liu: Data Curation, Formal Analysis, Investigation, Writing - Original Draft. **Peifang Wang:** Resources, Validation, Visualization. **Juan Chen:** Validation, Visualization. **Xin Gao:** Formal analysis. **Huinan Che:** Formal Analysis, Investigation, Methodology, Validation, Writing - Review & Editing. **Xiaozhi Su:** Testing, Project Administration. **Bin Liu:** Conceptualization, Investigation, Writing - Review & Editing. **Yanhui Ao:** Data Curation, Funding Acquisition, Methodology, Project Administration, Software, Supervision, Writing - Review & Editing.

Declaration of competing interest

The authors declare that they have no known competing financial interests or personal relationships that could have appeared to influence the work reported in this paper.

Acknowledgements

We are grateful for the financial support from the Natural Science Foundation of China (51979081, 52100179), Fundamental Research Funds for the Central Universities (B200202103), National Science Funds for Creative Research Groups of China (No.51421006), PAPD and Photon Science Research center for Carbon Dioxide.

Appendix A. Supplementary data

Supplementary data to this article can be found online at https://doi.org/10.1016/j.ese.2024.100414.

References

[1] J.X. Zhong, H. Jiang, Z.L. Wang, Z.G. Yu, L.Z. Wang, J.F. Mueller, J.H. Guo, Efficient photocatalytic destruction of recalcitrant micropollutants using graphitic carbon nitride under simulated sunlight irradiation, Environ. Sci. Ecotechnol. 5 (2021) 100079.
[2] Z. Hajalifard, M. Mousazadeh, S. Khademi, N. Khademi, M.H. Jamadi, M. Sillanpaa, The efficacious of AOP-based processes in concert with electrocoagulation in abatement of CECs from water/wastewater, Npj Clean Water 6 (2023) 30.
[3] J. Miao, J. Song, J.Y. Lang, Y. Zhu, J. Dai, Y. Wei, M.C. Long, Z.P. Shao, B.X. Zhou, P.J.J. Alvarez, L.Z. Zhang, Single-atom MnN_5 catalytic sites enable efficient peroxymonosulfate activation by forming highly reactive Mn(IV)-Oxo species, Environ. Sci. Technol. 57 (2023) 4266–4275.
[4] X. Gao, P.F. Wang, H.N. Che, W. Liu, Y.H. Ao, Breaking interfacial charge transfer barrier by sulfite for efficient pollutants degradation: a case of $BiVO_4$, Npj Clean Water 6 (2023) 42.

[5] D. Xu, C.C. Li, J.Y. Liu, G.J. Liu, H.L. Zhu, H.P. Zhang, B. Yu, Y.H. Guo, PES/Fe_3S_4@NiO self-cleaning membrane with rapid catalysis for effective emulsion separation and dye degradation, J. Membr. Sci. 684 (2023) 121874.

[6] C.B. Xiao, J.L. Yuan, L.Y. Li, N.B. Zhong, D.J. Zhong, Q.H. Xie, H.X. Chang, Y.L. Xu, X.F. He, M. Li, Photocatalytic synergistic biofilms enhance tetracycline degradation and conversion, Environ. Sci. Ecotechnol. 14 (2023) 100234.

[7] G.H. Chen, W.Y. Dong, H.J. Wang, Z.L. Zhao, F. Wang, F.F. Wang, C. Nieto-Delgado, Carbamazepine degradation by visible-light-driven photocatalyst Ag_3PO_4/GO: mechanism and pathway, Environ. Sci. Ecotechnol. 9 (2022) 100143.

[8] G. Zhou, P.F. Wang, H. Li, R. Huang, B. Hu, Y.T. Liu, T.H. Li, Bimetallic-atom-hybridization-driven catalytic reaction kinetics and solar utilization to accelerate norfloxacin degradation, Appl. Catal. B Environ. 298 (2021) 120525.

[9] W. Liu, P.F. Wang, Y.H. Ao, J. Chen, X. Gao, B.H. Jia, T.Y. Ma, Directing charge transfer in a chemical-bonded $BaTiO_3$@ReS_2 Schottky heterojunction for piezoelectric enhanced photocatalysis, Adv. Mater. 34 (2022) 2202508.

[10] S.X. He, M.J. Shen, E.Y. Wu, R.L. Yin, M.S. Zhu, L.X. Zeng, Molecular structure on the detoxification of fluorinated liquid crystal monomers with reactive oxidation species in the photocatalytic process, Environ. Sci. Ecotechnol. 9 (2022) 100141.

[11] X.L. Guo, X.P. Zhao, X.F. Luo, Y.L. Pang, B. Tian, S.X. Liu, S.J. Li, J. Li, B. Strehmel, Z.J. Chen, A sustainable wood-based iron photocatalyst for multiple uses with sunlight: water treatment and radical photopolymerization, Angew. Chem. Int. Ed. (2023) e20231242.

[12] H.N. Che, P.F. Wang, J. Chen, X. Gao, B. Liu, Y.H. Ao, Rational design of donor-acceptor conjugated polymers with high performance on peroxydisulfate activation for pollutants degradation, Appl. Catal. B Environ. 316 (2022) 121611.

[13] X.B. Sun, Y. Pan, Y.Y. Song, W. Liu, L.D. Nghiem, Q.L. Wang, Z.Q. Cai, Ceftriaxone sodium degradation by carbon quantum dots (CQDs)-decorated C-doped α-BiO nanorods, Environ. Sci. Ecotechnol. 13 (2023) 100219.

[14] C. Dong, Y. Yang, X. Hu, Y. Cho, G. Jang, Y. Ao, L. Wang, J. Shen, J.H. Park, K. Zhang, Self-cycled photo-Fenton-like system based on an artificial leaf with a solar-to-H_2O_2 conversion efficiency of 1.46, Nat. Commun. 13 (2022) 4982.

[15] Y. Wu, J. Chen, H. Che, X. Gao, Y. Ao, P. Wang, Boosting $2e^-$ oxygen reduction reaction in garland carbon nitride with carbon defects for high-efficient photocatalysis-self-Fenton degradation of 2,4-dichlorophenol, Appl. Catal. B Environ. 307 (2022) 121185.

[16] X.Q. Huo, H. Yi, E. Almatrafi, D.S. Ma, Y.K. Fu, L. Qin, W. Xia, L. Xiang, F.H. Xu, H.C. Yan, C.Y. Zhou, G.M. Zeng, C. Lai, Insights into Fenton-like oxidation of oxytetracycline mediated by Fe-doped porous g-C_3N_4 nanomaterials: synthesis, performance and mechanism, Environ. Sci.: Nano 10 (2023) 1828–1841.

[17] J.K. Lin, L. Jiang, W.J. Tian, Y.Y. Yang, X.G. Duan, Y. Jiao, H.Y. Zhang, S.B. Wang, The structure-dependent mechanism of single-atom cobalt on macroporous carbon nitride in (photo-)Fenton-like reactions, J Mater. Chem. A 11 (2023) 13653–13664.

[18] M.Y. Qian, X.L. Wu, M.C. Lu, L.Z. Huang, W.X. Li, H.J. Lin, J.R. Chen, S.B. Wang, X.G. Duan, Modulation of charge trapping by island-like single-atom cobalt catalyst for enhanced photo-fenton-like reaction, Adv. Funct. Mater. 33 (2023) 2208688.

[19] J. Xu, Q. Zhang, X. Gao, P.F. Wang, H.N. Che, C.M. Tang, Y.H. Ao, Highly efficient Fe-III-initiated self-cycled Fenton system in piezo-catalytic process for organic pollutants degradation, Angew. Chem. Int. Ed. 62 (2023) e202307018.

[20] S. Jin, Y.F. Zhang, X.J. Du, Q. Huang, Z. Chen, Promoted photo-Fenton reactivity through electron transfer between non-contacted Au nanoparticles and Fe_2O_3 nanowires in a confined space, Environ. Sci.: Nano 10 (2023) 1482–1493.

[21] Y. Wu, H.N. Che, B. Liu, Y.H. Ao, Promising materials for photocatalysis-self-fenton system: properties, modifications, and applications, Small Struct 4 (2023) 2200371.

[22] Y.F. Zhou, M.C. Yu, Q.Y. Zhang, X.L. Sun, J.F. Niu, Regulating electron distribution of Fe/Ni-N_4P_2 single sites for efficient photo-Fenton process, J. Hazard Mater. 440 (2022) 129724.

[23] H. Ma, Y. He, P. Chen, H. Wang, Y.J. Sun, J.Y. Li, F. Dong, G.X. Xie, J.P. Sheng, Ultrathin Two-Dimensional Bi-Based photocatalysts: synthetic strategies, surface defects, and reaction mechanisms, Chem. Eng. J 417 (2021) 129305.

[24] S. Chen, D.L. Huang, M. Cheng, L. Lei, Y.S. Chen, C.Y. Zhou, R. Deng, B. Li, Surface and interface engineering of two-dimensional bismuth-based photocatalysts for ambient molecule activation, J Mater. Chem. A 9 (2021) 196–233.

[25] F. Chen, T.Y. Ma, T.R. Zhang, Y.H. Zhang, H.W. Huang, Atomic-level charge separation strategies in semiconductor-based photocatalysts, Adv. Mater. 33 (2021) 2005256.

[26] J. Xiong, J. Di, J.X. Xia, W.S. Zhu, H.M. Li, Surface defect engineering in 2D nanomaterials for photocatalysis, Adv. Funct. Mater. 28 (2018) 1801983.

[27] Y. Zhou, Y. Zhang, M. Lin, J. Long, Z. Zhang, H. Lin, J.C.S. Wu, X. Wang, Monolayered Bi_2WO_6 nanosheets mimicking heterojunction interface with open surfaces for photocatalysis, Nat. Commun. 6 (2015) 8340.

[28] X.L. Wu, S. Liu, Y. Li, M.J. Yan, H.J. Lin, J.R. Chen, S.J. Liu, S.B. Wang, X.G. Duan, Directional and ultrafast charge transfer in oxygen-vacancy-rich ZnO@Single-Atom cobalt core-shell junction for photo-fenton-like reaction, Angew. Chem. Int. Ed. (2023) e202305639.

[29] J.K. Lin, W.J. Tian, Z.Y. Guan, H.Y. Zhang, X.G. Duan, H. Wang, H.Q. Sun, Y.F. Fang, Y.P. Huang, S.B. Wang, Functional carbon nitride materials in photo-fenton-like catalysis for environmental remediation, Adv. Funct. Mater. 32 (2022) 2201743.

[30] X.Y. Li, J.Y. Hu, Y.P. Deng, T. Li, Z.Q. Liu, Z. Wang, High stable photo-Fenton-like catalyst of FeP/Fe single atom-graphene oxide for long-term antibiotic tetracycline removal, Appl. Catal. B Environ. 324 (2023) 122243.

[31] J. Ding, Z.Y. Teng, X.Z. Su, K. Kato, Y.H. Liu, T. Xiao, W. Liu, L.Y. Liu, Q. Zhang, X.Y. Ren, J.C. Zhang, Z.Y. Chen, O. Teruhisa, A. Yamakata, H.B. Yang, Y.Q. Huang, B. Liu, Y.M. Zhai, Asymmetrically coordinated cobalt single atom on carbon nitride for highly selective photocatalytic oxidation of CH_4 to CH_3OH, Chem 9 (2023) 1017–1035.

[32] Z. Teng, Q. Zhang, H. Yang, K. Kato, W. Yang, Y.-R. Lu, S. Liu, C. Wang, A. Yamakata, C. Su, B. Liu, T. Ohno, Atomically dispersed antimony on carbon nitride for the artificial photosynthesis of hydrogen peroxide, Nat. Catal. 4 (2021) 374–384.

[33] Z.P. Yu, Y.F. Li, A. Torres-Pinto, A.P. LaGrow, V.M. Diaconescu, L. Simonelli, M.J. Sampaio, O. Bondarchuk, I. Amorim, A. Araujo, A.M.T. Silva, C.G. Silva, J.L. Faria, L.F. Liu, Single-atom Ir and Ru anchored on graphitic carbon nitride for efficient and stable electrocatalytic/photocatalytic hydrogen evolution, Appl. Catal. B Environ. 310 (2022) 121318.

[34] Y. Chen, J. Lin, B.H. Jia, X.D. Wang, S.Y. Jiang, T.Y. Ma, Isolating single and few atoms for enhanced catalysis, Adv. Mater. 34 (2022) 2201796.

[35] H.X. Zhang, Q.L. Hong, J. Li, F. Wang, X.S. Huang, S.M. Chen, W.G. Tu, D.S. Yu, R. Xu, T.H. Zhou, J. Zhang, Isolated square-planar copper center in boron imidazolate nanocages for photocatalytic reduction of CO_2 to CO, Angew. Chem. Int. Ed. 58 (2019) 11752–11756.

[36] F. Chen, X.L. Wu, C. Shi, H. Lin, J. Chen, Y. Shi, S. Wang, X. Duan, Molecular engineering toward pyrrolic N-rich M-N_4 (M = Cr, Mn, Fe, Co, Cu) single-atom sites for enhanced heterogeneous fenton-like reaction, Adv. Funct. Mater. 31 (2021) 2007877.

[37] X. Li, X. Wen, J.Y. Lang, Y. Wei, J. Miao, X.C. Zhang, B.X. Zhou, M.C. Long, P.J.J. Alvarez, L.Z. Zhang, CoN_1O_2 single-atom catalyst for efficient peroxymonosulfate activation and selective cobalt(IV)=O generation, Angew. Chem. Int. Ed. (2023) e202303267.

[38] X.N. Li, X. Huang, S.B. Xi, S. Miao, J. Ding, W.Z. Cai, S. Liu, X.L. Yang, H.B. Yang, J.J. Gao, J.H. Wang, Y.Q. Huang, T. Zhang, B. Liu, Single cobalt atoms anchored on porous N-doped graphene with dual reaction sites for efficient fenton-like catalysis, J. Am. Chem. Soc. 140 (2018) 12469–12475.

[39] L. Su, P. Wang, X. Ma, J. Wang, S. Zhan, Regulating local electron density of iron single sites by introducing nitrogen vacancies for efficient photo-fenton process, Angew. Chem. Int. Ed. 60 (2021) 21261–21266.

[40] Z. Haiyin, Z. Ruiren, W. Pengfei, Z. Qixing, Selective hydroxyl generation for efficient pollutant degradation by electronic structure modulation at Fe sites, P Natl, Acad. Sci. USA 120 (2023) e2305378120.

[41] S.T. Liu, C. Wang, J.H. Wu, B.L. Tian, Y.M. Sun, Y. Lv, Z.Y. Mu, Y.X. Sun, X.S. Li, F.Y. Wang, Y.Q. Wang, L.Y. Tang, P. Wang, Y.F. Li, M.N. Ding, Efficient CO_2 electroreduction with a monolayer Bi_2WO_6 through a metallic intermediate surface state, ACS Catal. 11 (2021) 12476–12484.

[42] H. Huang, C. Zhou, X. Jiao, H. Yuan, J. Zhao, C. He, J. Hofkens, M.B.J. Roeffaers, J. Long, J.A. Steele, Subsurface defect engineering in single-unit-cell Bi_2WO_6 monolayers boosts solar-driven photocatalytic performance, ACS Catal. 10 (2019) 1439–1443.

[43] C.H. Lu, X.R. Li, Q. Wu, J. Li, L. Wen, Y. Dai, B.B. Huang, B.J. Li, Z.Z. Lou, Constructing surface plasmon resonance on Bi_2WO_6 to boost high-selective CO_2 reduction for methane, ACS Nano 15 (2021) 3529–3539.

[44] Y.W. Teh, C.C. Er, X.Y. Kong, B.J. Ng, S.T. Yong, S.P. Chai, Charge modulation at atomic-level through substitutional sulfur doping into atomically thin Bi_2WO_6 toward promoting photocatalytic CO_2 reduction, ChemSusChem 15 (2022) e202200471.

[45] J. Jiang, X. Wang, Y. Liu, Y. Ma, T. Li, Y. Lin, T. Xie, S. Dong, Photo-Fenton degradation of emerging pollutants over Fe-POM nanoparticle/porous and ultrathin g-C_3N_4 nanosheet with rich nitrogen defect: degradation mechanism, pathways, and products toxicity assessment, Appl. Catal. B Environ. 278 (2020) 119349.

[46] L.S. Zhang, X.H. Jiang, Z.A. Zhong, L. Tian, Q. Sun, Y.T. Cui, X. Lu, J.P. Zou, S.L. Luo, Carbon nitride supported high-loading Fe single-atom catalyst for activating of peroxymonosulfate to generate $^1O_2$ with 100 % selectivity, Angew. Chem. Int. Ed. 60 (2021) 21751–21755.

[47] X. Gao, J. Chen, H.N. Che, Y.H. Ao, P.F. Wang, Rationally constructing of a novel composite photocatalyst with multi charge transfer channels for highly efficient sulfamethoxazole elimination: mechanism, degradation pathway and DFT calculation, Chem. Eng. J 426 (2021) 131585.

[48] Y. Zhou, L. Zhou, Y. Zhou, M. Xing, J. Zhang, Z-scheme photo-Fenton system for efficiency synchronous oxidation of organic contaminants and reduction of metal ions, Appl. Catal. B Environ. 279 (2020) 1119365.

[49] Y. Zhao, Y. Zhao, R. Shi, B. Wang, G.I.N. Waterhouse, L.Z. Wu, C.H. Tung, T. Zhang, Tuning oxygen vacancies in ultrathin TiO_2 nanosheets to boost photocatalytic nitrogen fixation up to 700 nm, Adv. Mater. 31 (2019) 1806482.

[50] X.H. Jiang, L.S. Zhang, H.Y. Liu, D.S. Wu, F.Y. Wu, L. Tian, L.L. Liu, J.P. Zou, S.L. Luo, B.B. Chen, Silver single atom in carbon nitride catalyst for highly efficient photocatalytic hydrogen evolution, Angew. Chem. Int. Ed. 59 (2020) 23112–23116.

[51] H.N. Che, X. Gao, J. Chen, J. Hou, Y.H. Ao, P.F. Wang, Iodide-induced

fragmentation of polymerized hydrophilic carbon nitride for high-performance quasi-homogeneous photocatalytic H_2O_2 production, Angew. Chem. Int. Ed. 60 (2021) 25546–25550.
[52] W. Liu, P. Wang, J. Chen, X. Gao, H. Che, B. Liu, Y. Ao, Unraveling the mechanism on ultrahigh efficiency photocatalytic H_2O_2 generation for dual-heteroatom incorporated polymeric carbon nitride, Adv. Funct. Mater. 32 (2022) 2205119.
[53] K.L. Zhang, M. Dan, J.F. Yang, F.X. Wu, L.G. Wang, H. Tang, Z.Q. Liu, Surface energy mediated sulfur vacancy of $ZnIn_2S_4$ atomic layers for photocatalytic H_2O_2 production, Adv. Funct. Mater. 33 (2023) 2302964.
[54] X.M. Xu, Y.M. Zhang, Y. Chen, C.H. Liu, W.J. Wang, J.J. Wang, H.T. Huang, J.Y. Feng, Z.S. Li, Z.G. Zou, Revealing *OOH key intermediates and regulating H_2O_2 photoactivation by surface relaxation of Fenton-like catalysts, P Natl. Acad. Sci. USA 119 (2022) 2205562119.
[55] H.B. Zhang, S.W. Zuo, M. Qiu, S.B. Wang, Y.F. Zhang, J. Zhang, X.W. Lou, Direct probing of atomically dispersed Ru species over multi-edged TiO_2 for highly efficient photocatalytic hydrogen evolution, Sci. Adv. 6 (2020) 9823.